CAMBRIDGE
UNIVERSITY PRESS

Article

Enhancement of the adsorption properties of two natural bentonites by ion exchange: equilibrium, kinetics and thermodynamic study

Ali Boukhemkhem[1], Alejandro H. Pizarro[2] and Carmen B. Molina[2]* 🆔

[1]Laboratory Interactions Materials – Environment (LIME), University of Mohamed Seddik Ben Yahia, Jijel, 18000, Algeria and [2]Chemical Engineering Department, Faculty of Sciences, Universidad Autónoma de Madrid, Cantoblanco, 28049, Madrid, Spain

ABSTRACT

In this investigation, Maghnia (Ma) and Mostaganem (Ms) bentonite clays, mined from west Algeria, with no prior affinity for anionic dyes, were modified by simple ion exchange with aqueous Fe^{3+} solutions, followed by calcination at 500°C. The resulting materials, Fe-Ma and Fe-Ms, respectively, were employed as adsorbents for methyl orange. The starting materials and the two adsorbents were characterized by X-ray diffraction, N_2 adsorption–desorption isotherms, Brunauer–Emmett–Teller specific surface area and X-ray fluorescence and by determining the point of zero charge. The effects of various variables, such as initial dye concentration, contact time, adsorbent dose, initial pH and adsorption temperature, were studied. The kinetics were well described by the pseudo-second-order model and the mechanism was determined from the intraparticle diffusion model, while corresponding isotherms fitted better to the Freundlich model. Thermodynamic parameters showed that the adsorption process was endothermic, spontaneous and physical in nature, accompanied by an increase of entropy.

Water pollution is a major environmental problem. Various pollutants are detected in industrial effluents and natural water bodies. Among these pollutants, synthetic dyes are discharged into the environment from various sources. They are generated by many industries such as textile, leather, food processing, tanning, cosmetics, paper and dye manufacturing (Li *et al.*, 2017). There exist more than 10,000 types of commercially available dyes with >0.7 million tons of dyestuff produced annually, and ~15% of this amount is lost in the final effluents, with 2% discharged directly into the aqueous effluents and 10% lost during dyeing operations (Soloman *et al.*, 2009). These pollutants represent a serious hazard to human health and to the ecosystem (Mouni *et al.*, 2018). Furthermore, their complex aromatic structures render them highly stable and difficult to remove from water matrices (Li *et al.*, 2017; Mobarak *et al.*, 2018). Their presence in water, even at very low concentrations, may inhibit oxygen and sunlight breakthrough, damaging the aquatic environment. Methyl orange (MO) is one of the well-known acidic monoazo dyes. It is widely used in printing, research and in the textile industry.

Several methods have been applied to remove these compounds from water, such as chemical precipitation, solvent extraction, evaporation, distillation, membrane filtration, reverse

osmosis, ion exchange, coagulation/flocculation, adsorption and electrochemical processes (De Castro *et al.*, 2018; Mouni *et al.*, 2018). Although most of these methods are efficient, they are often expensive and produce secondary waste products. Among all of these techniques, adsorption seems to be very promising, as it is inexpensive, simple to perform, requires little energy input and produces relatively little sludge (Nadaroglu *et al.*, 2015; Zhang *et al.*, 2015; He *et al.*, 2018). Adsorption of MO dye on activated carbon materials has been widely studied due to the effectiveness and versatility of these materials (Chen *et al.*, 2010; Huo *et al.*, 2013; Leon *et al.*, 2015). However, lower-cost, naturally occurring materials have also been tested as adsorbents (Liu *et al.*, 2009; Trevino-Cordero *et al.*, 2013). In addition, there has been increasing interest in the potential application of various clays, after appropriate modifications, as adsorbents in the removal of MO from water. These include kaolin (Zhu *et al.*, 2010; Tang *et al.*, 2017), vermiculite (Zang *et al.*, 2017), rectorite (Zhang *et al.*, 2011) and halloysite (Chen *et al.*, 2015). Bentonite, consisting mainly of smectite, has been studied extensively and used widely in industry due to its high availability, low cost and good adsorption capacity (Chen *et al.*, 2011; Leodopoulos *et al.*, 2012; Luo *et al.*, 2015; Zhang *et al.*, 2015; Belhouchat *et al.*, 2017; De Castro *et al.*, 2018). Smectite belongs to the 2:1 group of aluminosilicates, with its unit layer structure being one AlO_6 octahedral sheet sandwiched between two SiO_4 tetrahedral sheets. Its surface carries a permanent negative charge due to the isomorphic substitution of Si^{4+} by Al^{3+} in the tetrahedral sheet and the substitution of Al^{3+} by Mg^{2+} or Fe^{2+} in the octahedral sheet. This makes bentonite ineffective at adsorbing

*E-mail: carmenbelen.molina@uam.es

anionic dyes due to the repulsive interactions between the negatively charged surface and dye molecules (Khenifi *et al.*, 2007; Guo *et al.*, 2012).

Various methods have been proposed in the literature with regards to modifying clays in order to improve their affinity towards anionic dyes. The first such method involves pillaring through the intercalation of various polyoxocations to increase microporosity, potential active sites and specific surface area (Gil *et al.*, 2011; Hao *et al.*, 2014). The second such method involves organophilization with cationic surfactants such as cetyltrimethyl ammonium bromide (CTAB) through ion exchange, changing the clay surface from organophobic to strongly organophilic, thereby improving the adsorption capacity (Chen *et al.*, 2011; Guo *et al.*, 2012; Mobarak *et al.*, 2018).

To the authors' knowledge, no studies exist in the literature using only a simple ion-exchange method with inorganic cations, such as Fe^{3+}, followed by a calcination step in order to improve the adsorption affinity of bentonite towards anionic dyes such as MO. The current work aimed to investigate the improvement of MO dye adsorption onto two Na-bentonites extracted from two different deposits located in west Algeria. This approach is based on the transformation of the negative charge of the bentonite surface to a positive charge after Fe^{3+} adsorption and on an ion-exchange process between sodium cations located in the interlayer space and ferric cations transformed into iron oxide after calcination, giving rise to improved textural properties such as specific surface area and mesoporosity. Various variables such as initial dye concentration, contact time, adsorbent dose, initial pH and adsorption temperature were tested.

Materials and methods

Chemicals

The Maghnia and Mostaganem bentonite clays (Ma and Ms, respectively) were obtained from BENTAL (Société des bentonites d'Algérie). They were used as received without further treatment. All chemicals used in this study were of analytical grade. The anionic dye, MO ($pK_a = 3.4$, solubility in water at 20°C = 5.2 g L^{-1}) (Fig. 1), iron (III) chloride hexahydrate $(FeCl_3)6H_2O$, hydrochloric acid (HCl) and sodium hydroxide (NaOH) were purchased from Sigma-Aldrich. The pH of the reaction media was adjusted with 0.1 M HCl or NaOH aqueous solutions. Methyl orange solutions of various concentrations were prepared by diluting the stock solution to the desired concentration using deionized water. Deionized water from a Millipore Milli-Q system (18 MΩ cm^{-1}) was used in all experiments.

Preparation of adsorbents

The two adsorbents were prepared using an ion-exchange process, adding 2 g of Ma or Ms to 100 mL of an aqueous solution containing 1 g of $(FeCl_3)6H_2O$ and maintaining the mixture under vigorous stirring for 24 h at ambient temperature. Then, the
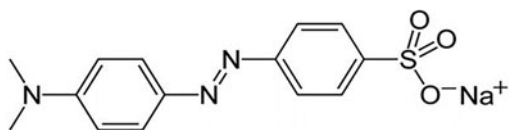

Fig. 1. MO molecular structure.

solid was washed with deionized water by centrifugation. The washing procedure was repeated until the supernatant was free of chlorides (conductivity of <10 μS cm^{-1}). After drying at 110°C, the product was calcined at 500°C for 2 h (Fig. S1) (Boukhemkhem *et al.*, 2019). The adsorbents are referred to hereafter as Fe-Ma and Fe-Ms, respectively.

Characterization methods

The chemical composition of the raw and modified bentonite clays was analysed by total reflection X-ray fluorescence (XRF) spectrometry using a TXRF EXTRA-II XRF spectrometer (after digestion of the solid samples by acid treatment at 100°C). The textural properties of the raw bentonite clays and the prepared adsorbents were determined by N_2 adsorption–desorption at –196°C using a Micromeritics Tristar 3020 instrument. The samples were previously outgassed overnight at 160°C under a residual pressure of 5×10^{-3} torr. The specific surface area was calculated according to the Brunauer–Emmett–Teller (BET) equation in the linear region of the relative pressure. The micropore volume was calculated using the t-plot method. The X-ray diffraction (XRD) traces of the materials were obtained with a Siemens D5000 diffractometer using Cu-$K\alpha$ radiation. The powder samples were scanned continuously at a scanning speed of 0.05° s^{-1} in the range 5–80°2θ. The point of zero charge of the adsorbents was determined using the pH-drift method (Issa *et al.*, 2014).

Adsorption experiments

All adsorption experiments were carried out in batch mode, under stirring at 400 rpm. The adsorption kinetic study was performed in a 1 L double-jacketed vessel at constant temperature (20°C). A total of 0.5 g of the adsorbent (Fe-Ms or Fe-Ma) was added to 500 mL of MO aqueous solution at various initial concentrations. Samples were removed from the reaction medium for various periods of time of between 5 and 120 min. This study was the only one in which 500 mL of the initial volume was employed, as the number of samples was large. The study of the effects of other variables was carried out in 100 mL flasks containing 50 mL of MO dye solution, with an initial MO concentration of 10 mg L^{-1}. In this case, a smaller volume of MO solution was used (50 mL) as the number of samples was three (results in triplicate) after 2 h of contact. The effect of the adsorbent dose was tested by using various amounts of the adsorbent, varying from 0.2 to 8.0 g L^{-1}. The effect of the initial pH of the solution was tested at various pH values between 3.0 and 10.5. The effect of temperature and the thermodynamic studies were performed at three different temperatures (20, 30 and 40°C). In the above experiments (initial pH and temperature effect), the adsorbent dose was 1 g L^{-1} as in the kinetic studies and the contact time was 2 h.

Adsorption isotherms were constructed from experiments performed in 100 mL flasks, where 0.05 g of the adsorbent were added to 50 mL of aqueous MO (i.e. at an adsorbent dose of 1 g L^{-1}) at various initial concentrations (0.5–30 mg L^{-1}) and at a contact time of 2 h. These experiments were performed at the optimal pH of 3.1 to obtain the maximum adsorption capacity of both adsorbents for the MO dye. The MO residual concentration was determined by UV–visible spectrophotometry (Agilent Cary 60) at a wavelength of 465 nm for pH >4.3 and at 500 nm at below that pH value, as the colour of solution changed with pH.
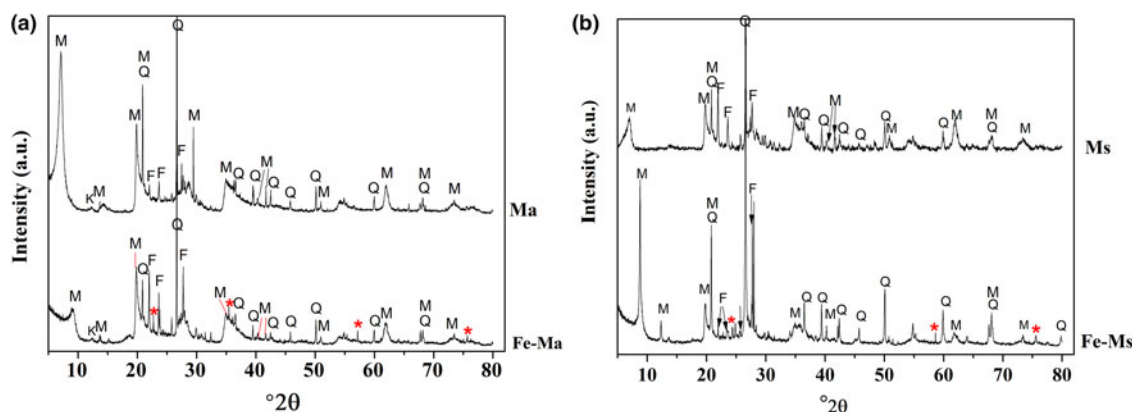
Fig. 2. XRD traces of (a) Ma and Fe-Ma and (b) Ms and Fe-Ms. M = montmorillonite; Q = quartz; F = feldspar; K = kaolinite; * = hematite.

Results and discussion

Characterization of adsorbents

The XRD traces of Ma and Ms before and after iron loading are shown in Fig. 2. The main phase is montmorillonite (M), and common impurities are feldspar (F), kaolinite (K) and quartz (Q), identified according to the JCPDS database. Sample Ma contains traces of kaolinite. When comparing the XRD traces of Fe-Ma and Fe-Ms with those of the corresponding raw bentonite clays, the layered structure was preserved in both modified materials. Thus, ion exchange with iron followed by calcination at 500° C affected only the layer stacking, as the basal peaks (001) were present with only slight displacement. In addition, some weak peaks, associated with α-Fe_2O_3, are present in the Fe-Ma and Fe-Ms XRD traces. Hence, there is evidence of iron oxide as α-Fe_2O_3 after treatment of Ma and Ms (Daud & Hameed, 2010; Hassan & Hameed, 2011).

Table 1 shows the elemental compositions of the raw and modified bentonite clays. The iron content increased significantly after impregnation, from 1.2% to 4.9% and from 2.8% to 8.6% for Ma and Ms, respectively. The differences between the amounts of iron incorporated into the clay structure in both bentonites may be explained by their various adsorbent properties.

Figure 3 depicts the N_2 adsorption–desorption isotherms. Nitrogen adsorption increased considerably after iron impregnation and calcination.

According to the International Union of Pure and Applied Chemistry (IUPAC) classification, the N_2 adsorption–desorption isotherms of the four samples may be classified as type IV with clear H3-type hysteresis loops, along with clear differences between the original and treated samples (Tomic et al., 2011). This type of isotherm is common for aggregates of plate-like

particles, with slit-shaped pores typical of clay minerals (Auta & Hameed, 2012). Such hysteresis loops are indicative of a high relative contribution of mesoporosity, which is more significant in Fe-Ma and Fe-Ms due to the textural modifications after Fe exchange. Both modified clays also showed greater N_2 adsorption at low relative pressure, indicative of microporosity development after the ion-exchange process. The pore-size distribution for the original and the modified clays is depicted in Fig. 4.

Moderate broadening of the micropore size was observed after Fe inclusion, while no significant changes occurred in the mesopore-size distribution, although the mesopore volume was increased. The specific surface areas of the samples (Table 1) increased significantly upon Fe exchange, mostly affecting the so-called external or non-microporous area. An increase in the micropore size was observed in Fe-Ma (from 11 Å in the original Ma bentonite to 13 Å) due to the modification of the clay after Fe exchange (Fig. 4a). In addition, development in mesoporosity after Fe exchange was observed, as additional peaks appear in the 20–500 Å region, with the main mesopore sizes being ~250 and 350 Å for both materials (Fig. 4b). The same trend is also observed for Ms and Fe-Ms clays, with the presence of two peaks at ~11 Å and 12 Å for Ms and Fe-Ms, respectively (Fig. 4c,d). Further peaks occur at between 20 and 500 Å, with the appearance of an intense peak located at ~34 Å in Fe-Ms. This indicates the important development of mesopores after Fe exchange.

The textural properties listed in Table 1 show that the Fe exchange increased the specific surface area values for both adsorbents to 73 m^2 g^{-1} for Fe-Ms and to 68 m^2 g^{-1} for Fe-Ma. The external surface area values increased dramatically after Fe exchange from 37 to 64 m^2 g^{-1} in Ma bentonite and from 20 to 57 m^2 g^{-1} in Ms bentonite. This may be attributed to the incorporation of Fe^{3+} in the interlayer space after ion exchange, increasing the micropore size after its transformation into α-Fe_2O_3. At the same time, part of α-Fe_2O_3 formed as a discrete phase outside of the interlayer space, probably contributing to the modification of the net negative charge on the surfaces of Fe-Ms and Fe-Ma (Chen & Zhu, 2009). The improvement in textural properties (specific surface area, pore size) and the modification of surface properties might improve the adsorption capacity of the bentonites.

The pH at the potential of zero-point charge (pH_{zpc}) values of the raw and modified bentonite clays are listed in Table 1. An important increase in pH_{zpc} values after Fe^{3+} ion exchange can be observed due to a significant reduction in surface negative charge, leading to a broadening in the pH range for the

Table 1. Textural properties and elemental compositions of the raw bentonite clays (Ma and Ms) and the prepared adsorbents (Fe-Ma and Fe-Ms).

Samples	pH_{zpc}	S_{BET} (m^2 g^{-1})	External surface area (m^2 g^{-1})	V_p (cm^3 g^{-1})	$V_{\mu p}$ (cm^3 g^{-1})	Si (mass%)	Al (mass%)	Fe (mass%)
Ma	4.0	55	37	0.077	0.0051	27.5	7.8	1.2
Fe-Ma	9.6	73	64	0.116	0.0064	21.7	6.7	4.9
Ms	4.2	22	20	0.046	0.0008	28.6	6.0	2.8
Fe-Ms	9.8	68	57	0.081	0.0046	23.0	4.9	8.6

S_{BET} = Brunauer–Emmett–Teller specific surface area; V_p = total pore volume; $V_{\mu p}$ = micropore volume.
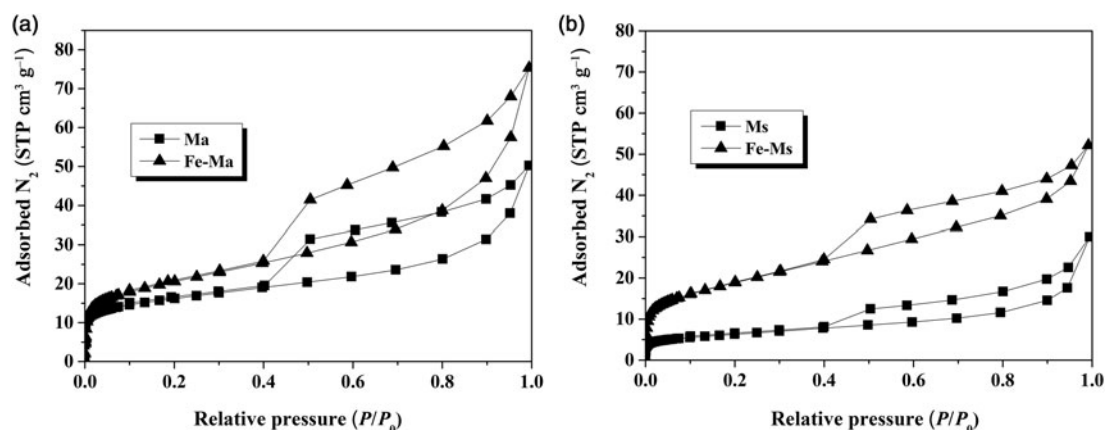
Fig. 3. N$_2$ adsorption–desorption isotherms of (a) Ma and Fe-Ma and (b) Ms and Fe-Ms. STP = standard conditions of temperature and pressure.

adsorption of anionic species (Gitari *et al.*, 2013). Thus, Fe-Ma and Fe-Ms show greater affinity towards MO than the original bentonite clays, which did not adsorb this anionic dye.

Effects of experimental parameters and kinetics

Effects of contact time and initial dye concentration. The original bentonite clays, Ma and Ms, showed almost negligible MO uptake

(results not shown). The evolution of the amount of MO adsorbed onto the two modified bentonite clays as a function of the contact time at various initial dye concentrations is shown in Fig. 5.

The adsorption of MO increased in Fe-Ma and Fe-Ms with increasing initial MO dye concentration. Using Fe-Ma, the quantity of MO adsorbed after 120 min of contact time increased from 2.76 to 7.04 mg g^{-1} when the initial MO concentration increased
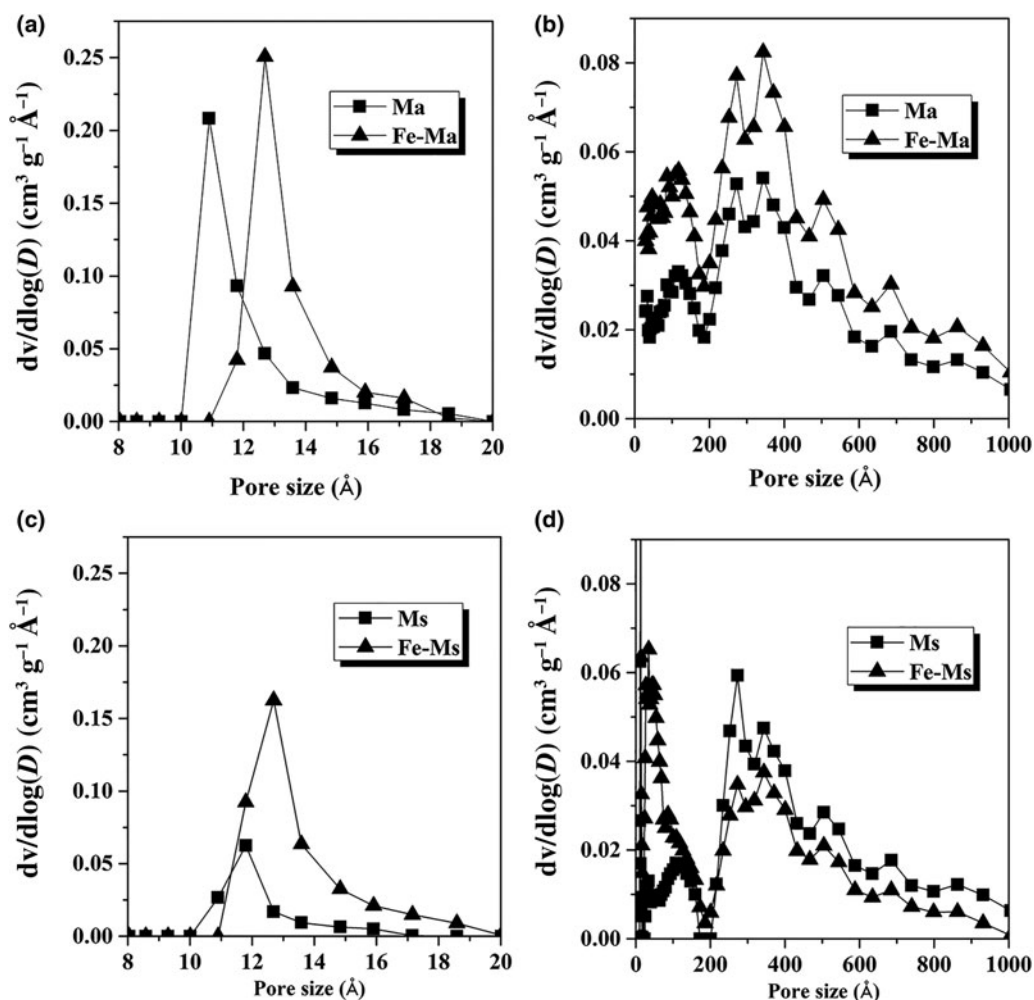

Fig. 4. Pore-size distributions according to the Barrett–Joyner–Halenda (BJH) method of (a, b) Ma and Fe-Ma and (c, d) Ms and Fe-Ms.
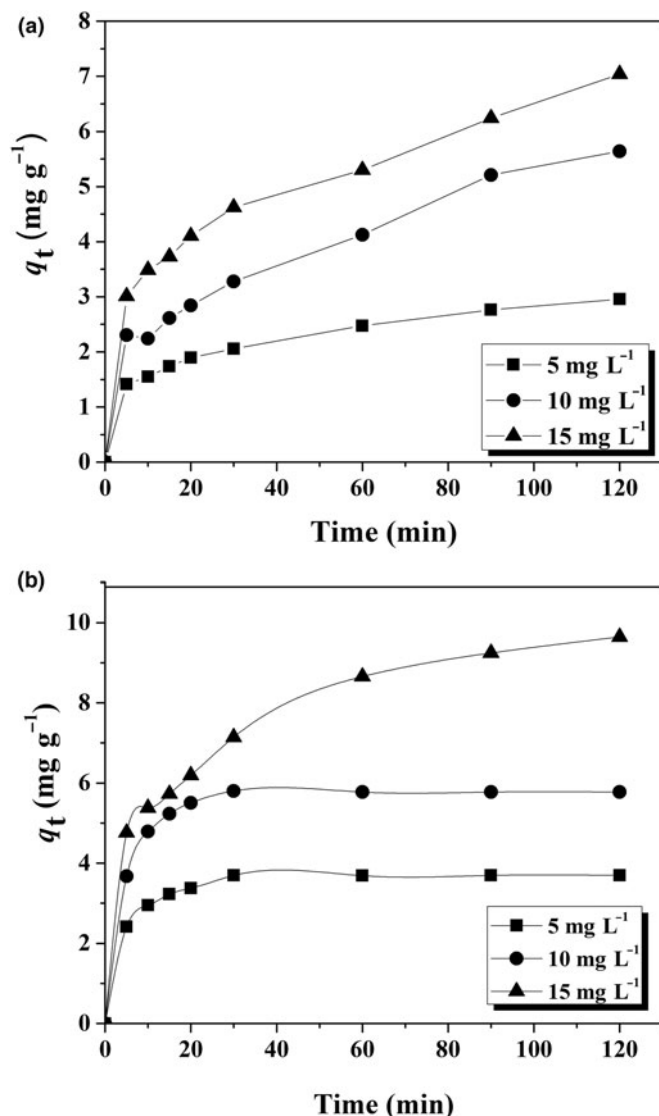
Fig. 5. Adsorption of MO onto (a) Fe-Ma and (b) Fe-Ms at various contact times and initial MO concentrations (adsorbent dose = 1 g L^{-1}, T = 20°C, pH$_i$ = 5.6, V = 500 mL, stirring speed = 400 rpm).

gradient between the aqueous and the solid phases also contribute to these results (Kushwaha *et al.*, 2011; Auta & Hameed, 2012; Nadaroglu *et al.*, 2015; Zhang *et al.*, 2015). The time required to reach equilibrium depends on the type of adsorbent and the initial dye concentration. In the case of MO adsorption on Fe-Ms, the equilibrium time was ~30 min for initial dye concentrations of 5 and 10 mg L^{-1}. For the highest concentration of 15 mg L^{-1}, the equilibrium was attained at a significantly longer contact time of ~90 min. However, in Fe-Ma, 60 and 90 min were necessary to attain equilibrium for concentrations of 5 and 10 mg L^{-1}, respectively. Nevertheless, equilibrium was not reached after 120 min with an initial concentration of 15 mg L^{-1}. This difference between the two systems may be attributed to the greater microporosity of Fe-Ma (Table 1).

The experimental curves of Fig. 5 were fitted to three models used to describe adsorption kinetics: the pseudo-first-order kinetic model (Eq. 1), the pseudo-second-order kinetic model (Eq. 2) and the intraparticle diffusion model (Eq. 3). These models are expressed in their linear forms as follows, respectively:

$$\ln(q_e - q_t) = \ln q_e - k_1 t \qquad (1)$$

$$\frac{t}{q_t} = \left(\frac{1}{k_2 q_e^2}\right) + \left(\frac{1}{q_e}\right)t \qquad (2)$$

$$q_t = k_{int} t^{1/2} + I \qquad (3)$$

where q_e and q_t (mg g^{-1}) are the amounts adsorbed at equilibrium and time t (min), respectively, k$_1$ (min^{-1}) is the pseudo-first-order rate constant, k$_2$ (g mg^{-1}·min^{-1}) is the pseudo-second-order rate constant, k$_{int}$ (mg g^{-1} min$^{-0.5}$) is the intraparticle diffusion rate constant and I (mg g^{-1}) is the intercept. The corresponding fitting parameters for the three models are listed in Table 2.

The pseudo-first-order model did not describe adequately the adsorption kinetics due to the low values of the coefficients of determination R^2, which varied between 0.79 and 0.97, and the calculated adsorption capacities ($q_{1,cal}$), which were rather small compared to the experimental adsorption capacities ($q_{1,exp}$) (Table 2). However, the pseudo-second-order model provided an excellent fit for both systems and for the three concentrations, as the coefficients of determination were considerably higher than those obtained using the pseudo-first-order model. Moreover, the calculated adsorption capacities using this model ($q_{2,cal}$) were comparable to the experimental adsorption capacities ($q_{2,exp}$). Therefore, it can be inferred that the pseudo-second-order model showed good compliance with the experimental data. These results are in good agreement with others studies that showed that the adsorption of MO dye on modified montmorillonite is best described by the pseudo-second-order model (Luo *et al.*, 2015; Zhang *et al.*, 2015, Zang *et al.*, 2017).

In order to evaluate the influence of intraparticle diffusion on the rate of the adsorption process, a plot of q_t *vs* $t^{1/2}$ for both adsorbents at various initial dye concentrations was obtained (Fig. S2). These plots show the same general trend, with two stages (He *et al.*, 2016; Wan *et al.*, 2016; Mobarak *et al.*, 2018). These two stages (intraparticle diffusion and equilibrium) were identified for both systems, but for the adsorption of 15 mg L^{-1} MO on Fe-Ma there was no evidence of the final equilibrium stage. In addition, the intraparticle diffusion rate values (k$_{int}$) increased with increasing initial dye concentration for both systems (Table 2). This may be due to an increase in the driving

from 5 to 15 mg L^{-1} (Fig. 5a). The same tendency was also observed at the same contact time for the Fe-Ms as the adsorbent, as the amount of adsorbed MO increased from 3.69 to 9.25 mg g^{-1} in the same range of initial dye concentrations. This is attributed to an increase in the concentration gradient to the active sites of the adsorbents Fe-Ma and Fe-Ms, and to an enhancement of the interaction between the dye molecules and the active sites located on the surface and within the pores of the adsorbents (Auta & Hameed, 2012). The uptake of MO molecules at low contact times is very rapid, becoming gradually slower thereafter until equilibrium is established. This decrease in the adsorption rate is more pronounced in Fe-Ms (Fig. 5b). This trend in adsorption kinetics indicates that the number of active sites available on the surface of the adsorbent is much greater at the beginning of the adsorption. However, after 30 min of adsorption, the vacant sites are much fewer and, probably, difficult to access as they are located inside the adsorbent pores. Moreover, the competition between MO molecules and the reduction in the concentration

Table 2. Kinetic parameters for the adsorption of MO dye on Fe-Ma and Fe-Ms (adsorbent dose = 1 g L^{-1}, T = 20°C, pH$_i$ = 5.6, V = 500 mL, stirring speed = 400 rpm).

Kinetic model, pseudo-first-order	$q_{e,exp}$ (mg g^{-1})		k_1 (min^{-1})		$q_{1,cal}$ (mg g^{-1})		R^2	
	Fe-Ma	**Fe-Ms**	**Fe-Ma**	**Fe-Ms**	**Fe-Ma**	**Fe-Ms**	**Fe-Ma**	**Fe-Ms**
5 mg L^{-1}	2.95	3.70	0.040	0.118	2.02	2.87	0.79	0.94
10 mg L^{-1}	5.64	5.77	0.035	0.095	4.07	2.01	0.89	0.92
15 mg L^{-1}	7.04	9.64	0.020	0.032	4.85	6.86	0.92	0.97
Pseudo-second-order	$q_{e,exp}$ (mg g^{-1})		k_2 (g mg^{-1} min^{-1})		$q_{2,cal}$ (mg g^{-1})		R^2	
	Fe-Ma	**Fe-Ms**	**Fe-Ma**	**Fe-Ms**	**Fe-Ma**	**Fe-Ms**	**Fe-Ma**	**Fe-Ms**
5 mg L^{-1}	2.95	3.70	0.034	0.117	3.02	3.78	0.99	0.99
10 mg L^{-1}	5.64	5.77	0.007	0.094	6.34	5.89	0.97	0.99
15 mg L^{-1}	7.04	9.64	0.009	0.008	7.47	10.43	0.98	0.99
Intraparticle diffusion	Time (min)		k_{int} (mg L^{-1} min$^{-0.5}$)		I (mg g^{-1})		R^2	
	Fe-Ma	**Fe-Ms**	**Fe-Ma**	**Fe-Ms**	**Fe-Ma**	**Fe-Ms**	**Fe-Ma**	**Fe-Ms**
5 mg L^{-1}	5–60	5–20	0.244	0.215	0.80	0.91	0.99	0.97
10 mg L^{-1}	5–90	5–20	0.437	0.355	0.97	1.26	0.99	0.97
15 mg L^{-1}	5–120	5–60	0.449	0.439	2.04	2.09	0.99	0.99

force caused by the concentration gradient and, consequently, the diffusion into active sites within the pores is favoured. In all cases, the intraparticle diffusion plot did not pass through the origin, supporting the notion that intraparticle diffusion is involved in the control of the adsorption rate, but it is not the only limiting step, as some degree of boundary-layer contribution also impacts on the rate control of the process (Chen *et al.*, 2010). Moreover, with increasing concentration from 5 to 15 mg L^{-1}, the *I* values increased from 0.80 to 2.04 mg L^{-1} and from 0.91 to 2.09 mg L^{-1} for Fe-Ma and Fe-Ms, respectively. This increase suggests an abundance of adsorbed MO molecules on the boundary layer (Hamdaoui, 2006). From these results, the following scenario may be proposed: once the adsorption sites on the surface are occupied, adsorption continues and the molecules migrate towards the less easily accessible active sites located inside the pores, until all of the available active sites are occupied and the equilibrium is reached (He *et al.*, 2016).

Effects of adsorbent dosage. The effects of the Fe-Ms and Fe-Ma dosage on dye removal are shown in Fig. 6a.

At low adsorbent dose values (0.2–1.0 g L^{-1}), the removal efficiency increases considerably, from 18% to 56% and from 31% to 58% for Fe-Ma and Fe-Ms, respectively. This is attributed to the increase in specific surface area of the ion-exchanged materials with respect to the raw bentonite clays and the availability of additional adsorption sites. Using an adsorbent dose of 4 g L^{-1}, MO removal rates of 64% and 78% were observed for Fe-Ma and Fe-Ms, respectively. However, further increases of this dose did not affect the MO removal efficiency of the materials.

Effects of initial pH. The adsorption of MO dye onto Fe-Ma and Fe-Ms as a function of the initial pH of the dye solution was tested (Fig. 6b). The MO uptake decreased dramatically up to pH 7 and then the decreasing trend becomes progressively slower. An almost complete removal of dye from solution for both adsorbents was observed at pH 3.1. However, increases in the initial pH of the MO solution led to dramatic decreases in decolouration efficiency. At the highest pH value used of 10.2, the dye removal rates were only 20% and 6% for Fe-Ma and Fe-Ms, respectively. This behaviour can be explained by considering the pH$_{zpc}$ (Table 1). The surface of the adsorbent is positively charged at pH values lower than the pH$_{zpc}$ (~10), thus attracting the anionic MO. As the pH of the solution increases, the positive charge of the surface decreases, and so does the electrostatic interaction.
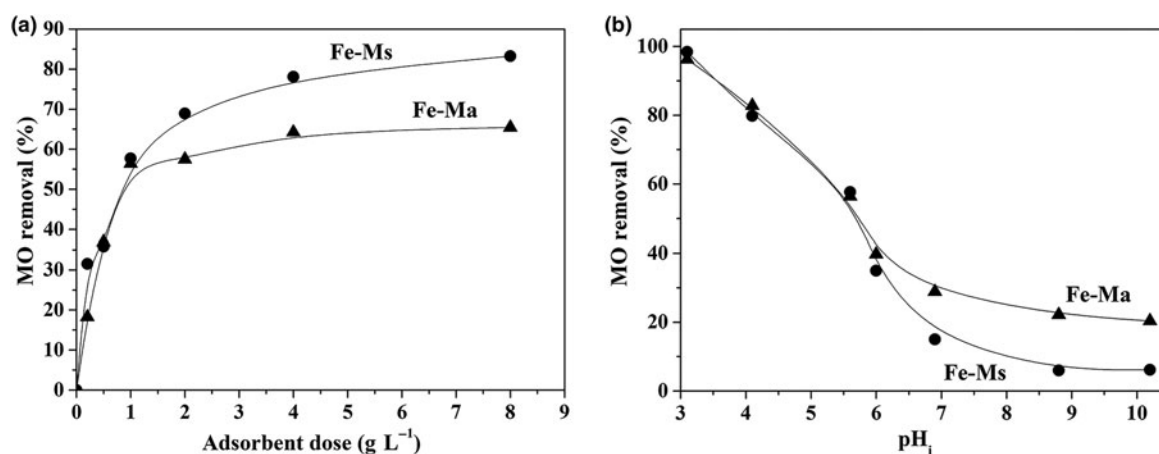

Fig. 6. Effect on MO removal efficiency of (a) adsorbent dosage (C_0 = 10 mg L^{-1}, T = 20°C, pH$_i$ = 5.6, V = 50 mL, t = 2 h, stirring velocity = 400 rpm) and (b) initial pH (C_0 = 10 mg L^{-1}, T = 20°C, adsorbent dose = 1 g L^{-1}, V = 50 mL, t = 2 h, stirring speed = 400 rpm).

Table 3. Temperature effects and thermodynamic parameters for adsorption of MO onto Fe-Ma and Fe-Ms ($C_0 = 10$ mg L^{-1}, $T = 20$–40°C, pH$_i$ = 5.6, adsorbent dose = 1 g L^{-1}, $t = 2$ h, stirring speed = 400 rpm).

	q_e (mg g^{-1})	ΔH^0 (kJ mol^{-1})	ΔS^0 (JK^{-1} mol^{-1})	ΔG^0 (kJ mol^{-1})
Fe-Ma				
20°C	5.6			−0.65
30°C	6.3	25.5	89.2	−1.54
40°C	7.1			−2.43
Fe-Ms				
20°C	5.8			−0.48
30°C	6.5	25.3	88.0	−1.36
40°C	7.2			−2.24

At pH values greater than the pH$_{zpc}$, the surface of the adsorbent presents a net negative charge (Zhu *et al.*, 2010). Thus, the electrostatic repulsive force between the surface and the anionic species of the MO molecules becomes dominant, weakening the adsorption of MO on both adsorbent surfaces. Moreover, the alkaline conditions increase the competition between OH and dye anions for adsorptive sites (Zhang *et al.*, 2015; Zang *et al.*, 2017).

Effects of temperature. The adsorption capacities of Fe-Ms and Fe-Ma at equilibrium were studied at 20, 30 and 40°C. The results obtained are listed in Table 3. With temperature increasing from 20 to 40°C, the amount of MO adsorbed at equilibrium increased from 5.6 to 7.1 mg g^{-1} for Fe-Ma and from 5.8 to 7.2 mg g^{-1} for Fe-Ms.

These results may reflect the endothermic nature of the MO retention of the two adsorbents. The increase in adsorption capacity with temperature may be attributed to the increasing mobility of MO molecules over the boundary layer and the internal pores of the adsorbent particles. Moreover, this increase can be attributed to an enlargement of the surface, probably due to the positive coefficient of the thermal expansion of the lattice structure for both adsorbents, as well as to an activation of the adsorbent surface (Almeida *et al.*, 2009; Arshadi *et al.*, 2016).

Equilibrium study
The adsorption isotherms are used to describe the distribution of the adsorbate molecules between the liquid and solid phases at equilibrium (Almeida *et al.*, 2009; Chen *et al.*, 2010; De Castro *et al.*, 2018). Several models have been employed to describe such isotherms. In this study, Langmuir (Eq. 4), Freundlich (Eq. 5) and Elovich (Eq. 6) models were used to fit the experimental data of the adsorption equilibria of MO on Fe-Ma and Fe-Ms.

$$\frac{1}{q_e} = \frac{1}{q_m K_L C_e} + \frac{1}{q_m} \tag{4}$$

$$\ln q_e = \frac{1}{n} \ln C_e + \ln K_F \tag{5}$$

$$\ln \frac{q_e}{C_e} = \left(-\frac{q_e}{q_m}\right) + \ln(K_E \times q_m) \tag{6}$$

where C_e is the MO concentration at equilibrium (mg L^{-1}), q_e is the amount adsorbed at equilibrium (mg g^{-1}), q_m is the monolayer adsorption capacity (mg g^{-1}), K_L is the Langmuir equilibrium constant (L mg^{-1}), K_F ((mg g^{-1})(L mg^{-1})$^{-1/n}$) and n is the Freundlich constant associated with the capacity and intensity of adsorption. In the case of 1/n < 1, the adsorption is considered
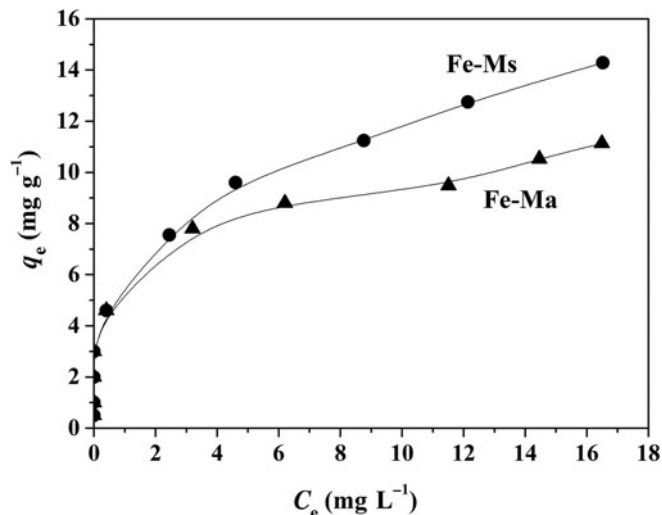

Fig. 7. Adsorption isotherms of MO on Fe-Ma and Fe-Ms ($C_0 = 0.5$–30 mg L^{-1}, adsorbent dose = 1 g L^{-1}, $T = 20$°C, pH$_i$ = 3.1, $V = 50$ mL, $t = 2$ h, stirring speed = 400 rpm).

favourable; otherwise, adsorption is considered difficult or unfavourable. Finally, K_E denotes the Elovich equilibrium constant (L mg^{-1}) (Ma *et al.*, 2013; Patrulea *et al.*, 2013; Tang *et al.*, 2017).

The isotherms for the adsorption of MO dye on Fe-Ma and Fe-Ms are presented in Fig. 7.

According to the Giles classification, the shapes of the isotherms (Fig. 7) belong to the L type (Giles *et al.*, 1960). This type of isotherm indicates high affinity between the adsorbent surface and the MO dye molecules. The adsorbed amount of MO dye increases with increasing initial dye concentration due to the driving force caused by an increase in the concentration gradient that overcomes the resistance of the dye molecule transport and improves the interaction between the active sites on the surface and within the pores and the MO molecules. However, the adsorption ability declines at greater MO concentrations due to the gradual saturation of the active sites on the two materials (Zhang *et al.*, 2015). The experimental adsorption capacities were 11.1 and 14.3 mg g^{-1} for Fe-Ma and Fe-Ms, respectively. It can be concluded that the introduction of iron into the interlayers of smectites in the bentonite clays Ms and Ma increased significantly the affinity for the MO dye due to modification of the

Table 4. Fitting parameters for the adsorption of MO onto Fe-Ma and Fe-Ms using various adsorption models (adsorbent dose = 1 g L^{-1}, $T = 20$°C, pH$_i$ = 3.1, $V = 50$ mL, $t = 2$ h, stirring speed = 400 rpm).

	Fe-Ma	Fe-Ms
Langmuir		
q_m (mg g^{-1})	11.43	15.44
K_L (L mg^{-1})	0.64	0.38
R^2	0.86	0.97
Freundlich		
1/n	0.23	0.30
K_F ((mg g^{-1})(L mg^{-1})$^{-1/n}$)	5.75	5.96
R^2	0.99	0.99
Elovich		
q_m (mg g^{-1})	2.19	3.81
K_E (L mg^{-1})	7.41	1.86
R^2	0.96	0.93

Table 5. Comparison of adsorption capacities for MO of the Fe-Ma and Fe-Ms clays with other materials reported in the literature.

Adsorbent	pH_i	T (°C)	Adsorbent dose (g L^{-1})	Contact time	q_m (mg g^{-1})	Reference
CTAB/chitosan/bentonite	NR	25	1.25	3 h	102.0	Guo *et al.* (2012)
Granular activated carbon	5.7	40	0.5	24 h	46.0	Leon *et al.* (2015)
Acid-activated bentonite	NR	25	2.0	NR	33.8	Leodopoulos *et al.* (2012)
Zr(IV)-chitosan/bentonite	Natural	30	0.6	5 h	438.6	Zhang *et al.* (2015)
Chitosan/rectorite/Fe_3O_4	NR	25	4.0	80 min	5.5	Zeng *et al.* (2015)
Gemini-modified bentonite	NR	25	2.0	2 h	161.0	Luo *et al.* (2015)
Magnetic/maghemite/chitosan nanocomposite	NR	57	1.0	NR	29.4	Jiang *et al.* (2012)
Chitosan beads	8.0	22	100	72 h	5.6	Morais *et al.* (2008)
Activated carbon from *Prosopis juliflora*	NR	30	1.0	50 min	10.3	Kumar & Tamilarasan (2013)
Cross-linked chitosan/bentonite	Natural	20	0.6	2 h	225.0	Huang *et al.* (2015)
Calcium alignate–carbon nanotubes	7.0	298	NR	2 h	12.5	Sui *et al.* (2012)
Magnetic alignate beads	7.5	NR	2.5	48 h	6.5	Rocher *et al.* (2010)
Fe_2O_3/Maghnia bentonite	3.1	20	1.0	2 h	11.4	Current work
Fe_2O_3/Mostaganem bentonite	3.1	20	1.0	2 h	15.4	Current work

NR = not reported.

textural properties, creating active sites on the clay layers after ion exchange and because of the change in the pH_{zpc} of the smectite surfaces (Table 1).

Table 4 lists the parameters for each model used to describe such adsorption isotherms. The Freundlich model provides the best fit to the experimental data for both adsorbents according to the coefficients of determination (R^2). It is possible that neither system followed a homogenous adsorption mechanism where an adsorption site becomes unavailable to other molecules once a molecule has been adsorbed on it, thus making it possible to continue adsorption. In this case, the adsorption is considered to be favourable, as the heterogeneity factor (1/n) for both adsorbents was <1 and multilayer adsorption of MO on the active heterogeneous surface is very possible. This active energetic heterogeneity can be attributed to the modification of the surface properties of Ms and Ma after Fe exchange, leading to some irregularity in pore shape, pore size, functional groups and surface charge (Auta & Hameed, 2012).

Regarding the Elovich model, very different values of maximum adsorption capacity were observed: those determined using the linear model equation are much lower than the experimental adsorbed amounts at equilibrium, in spite of the good coefficient of determination. Therefore, the Elovich model is unable to describe the adsorption isotherms of MO over Fe-Ma and Fe-Ms. This result is an indication that the process is probably dominated by physisorption (Hamdaoui & Naffrechoux, 2007). This physical nature is probably due to weak electrostatic interactions between the positive charges on the surface and the negative charge of the sulfonic group of the MO molecule.

Thermodynamics of adsorption

Thermodynamic parameters for adsorption such as ΔH^0 and ΔS^0 can be calculated using the van't Hoff equation (Eq. (7)):

$$\ln K_d = \frac{\Delta S^0}{R} - \frac{\Delta H^0}{RT} \tag{7}$$

while the Gibbs free energy is determined using Eq. (8):

$$\Delta G^0 = \Delta H^0 - T\Delta S^0 \tag{8}$$

where K_d is the distribution coefficient, which is equal to $q_e m/C_e$ (with m being the adsorbent dose in g L^{-1}), ΔH^0 (kJ mol^{-1}) and

ΔS^0 (J mol^{-1}) are, respectively, the standard enthalpy and the standard entropy, ΔG^0 represents the Gibbs free energy (kJ mol^{-1}), T (K) is the absolute temperature and R (J K^{-1} mol^{-1}) is the universal ideal gas constant (Kushwaha *et al.*, 2011). The calculated values of these three parameters for various adsorption temperatures are reported in Table 3.

The positive values of ΔH^0 for both systems indicate the endothermic nature of the process. The negative values of ΔG^0 for the three adsorption temperatures indicate the spontaneity and feasibility of the process. Furthermore, the increase in negative values of ΔG^0 at higher adsorption temperatures is indicative of rapid and more spontaneous adsorption. The positive values of ΔS^0 indicate that the degree of randomness at the solid–liquid interface increased with increasing temperature. In addition, the physical nature of the process is confirmed by ΔG^0 values ranging between 0 and –20 kJ mol^{-1} and by the ΔH^0 values being <80 kJ mol^{-1} for both systems (Almeida *et al.*, 2009; Auta & Hameed, 2012).

Comparison with other adsorbents

A comparison of the MO monolayer adsorption capacities on Fe-Ma and Fe-Ms with other adsorbents reported in the literature is shown in Table 5. All of these data come from experiments conducted at optimal initial pH values, except in those in which the pH values have been not reported.

The adsorption capacities of the two adsorbents prepared in this work were greater than those of the other materials reported in the literature, such as a chitosan/rectorite/Fe_2O_3 composite, chitosan beads, activated carbon derived from *Prosopis juliflora* biomass and magnetic alignate beads. They also have almost identical adsorption capacities to calcium alignate–carbon nanotube composites. However, some other adsorbents reported in Table 5 show greater adsorbent capacities, which may be attributed to the transformation of the clay surface from organophobic to strongly organophilic, modifying the global charge, the availability of more functional groups and the textural properties. Therefore, Fe-Ma and Fe-Ms, low-cost and easily prepared adsorbents, seem to be suitable for MO dye removal, as their adsorption capacities were similar to those obtained for the other low-cost adsorbents reported in Table 5.

Conclusions

Two inexpensive adsorbents were prepared by ion exchange with an $FeCl_3$ solution followed by calcination of the Ma and Ms

bentonites. The textural properties of both bentonite clays, such as specific surface area, pore volume and micropore/mesopore distribution, were greatly improved without any significant change to their structure, except for the presence of characteristic peaks of iron oxide, α-Fe$_2$O$_3$, in the XRD traces. The net negative surface charges of the two starting clays were significantly affected, as both adsorbents yielded larger values of pH$_{zpc}$ than the raw bentonite clays. These modifications were effective at providing both bentonite clays with significant affinity to the anionic dye MO. The maximum percentage of dye removal was observed at an initial pH of $\sim$3, temperatures of up to 40°C and an adsorbent dose of 4 g L^{-1}. The adsorption capacity of both adsorbents increased with increasing contact time and initial dye concentration. Favourable L-type isotherms were better described by the Freundlich model rather than by the Langmuir model. The adsorption kinetics fitted well to the pseudo-second-order model, and intraparticle diffusion was involved in the control of the adsorption rate. The thermodynamic study revealed the physical nature of the uptake of MO dye on Fe-Ma and Fe-Ms, which was endothermic, spontaneous and accompanied by an increase in entropy. Hence, Fe-Ma and Fe-Ms may be used as effective MO adsorbents due to the low cost and natural occurrence of the raw bentonites and their relatively large adsorption capacity.

References

Almeida C.A.P., Debacher N.A., Downs A.J., Cottet L. & Mello C.A.D. (2009) Removal of methylene blue from colored effluents by adsorption on montmorillonite clay. *Journal of Colloid Interface Science*, **332**, 46–53.

Arshadi M., Mousavinia F., Amiri M.J. & Faraji A.R. (2016) Adsorption of methyl orange and salicylic acid on a nano-transition metal composite: kinetics, thermodynamic and electrochemical studies. *Journal of Colloid Interface Science*, **483**, 118–131.

Auta M. & Hameed B.H. (2012) Modified mesoporous clay adsorbent for adsorption isotherm and kinetics of methylene blue. *Chemical Engineering Journal*, **198–199**, 219–227.

Belhouchat N., Zaghouane-Boudiaf H. & Viseras C. (2017) Removal of anionic and cationic dyes from aqueous solution with activated organo-bentonite/sodium alginate encapsulated beads. *Applied Clay Science*, **135**, 9–15.

Boukhemkhem A., Rida K., Pizarro A.H., Molina C.B. & Rodriguez J.J. (2019) Fe catalyst supported on modified kaolin for catalytic wet peroxide oxidation. *Clay Minerals*, **54**, 67–73.

Chen H., Yan H., Pei Z., Wu J., Li R., Jin Y. & Zhao J. (2015) Trapping characteristic of halloysite lumen for methyl orange. *Applied Surface Science*, **347**, 769–776.

Chen J. & Zhu L. (2009) Comparative study of catalytic activity of different Fe-pillared bentonites in the presence of UV light and H$_2$O$_2$. *Separation and Purification Technology*, **67**, 282–288.

Chen S., Zhang J., Zhang C., Yue Q., Li Y. & Li C. (2010) Equilibrium and kinetic studies of methyl orange and methyl violet adsorption on activated carbon derived from *Phragmites australis. Desalination*, **252**, 149–156.

Chen Z., Jin X., Chen Z., Megharaj M. & Naidu R. (2011) Removal of methyl orange from aqueous solution using bentonite-supported nanoscale zerovalent iron. *Journal of Colloid Interface Science*, **363**, 601–607.

Daud N.K. & Hameed B.H. (2010) Decolorization of acid red 1 by Fenton-like process using rice husk ash-based catalyst. *Journal of Hazardous Materials*, **176**, 938–944.

De Castro M.L.F.A., Abad M.L.B., Sumalinog D.G., Abarca R.R.M., Paoprasert P. & de Luna M.D.G. (2018) Adsorption of methylene blue dye and Cu(II)

ions on EDTA-modified bentonite: isotherm, kinetics and thermodynamic studies. *Environment, Development and Sustainability*, **5**, 197–205.

Gil A., Assis F.C.C., Albeniz S. & Korili S.A. (2011) Removal of dyes from wastewaters by adsorption on pillared clays. *Chemical Engineering Journal*, **168**, 1032–1040.

Giles C., MacEwan T. & Nakhwa S.N. (1960) Studies in adsorption. Part XI. A system of classification of solution adsorption isotherms and its use in diagnosis of adsorption mechanisms and in measurement of specific surface areas of solids. *Journal of the Chemical Society*, 3973–3993.

Gitari W.M., Ngulube T., Masindi V. & Gumbo J.R. (2013) Defluoridation of groundwater using Fe^{3+} modified bentonite clay: optimization of adsorption conditions. *Desalination and Water Treatment*, **53**, 1578–1590.

Guo J., Chen S., Liu L., Li B., Yang P., Zhang L. & Feng Y. (2012) Adsorption of dye from wastewater using chitosan–CTAB modified bentonites. *Journal of Colloid Interface Science*, **382**, 61–66.

Hamdaoui O. (2006) Batch study of liquid-phase adsorption of methylene blue using cedar sawdust and crushed brick. *Journal of Hazardous Materials*, **B135**, 264–273.

Hamdaoui O. & Naffrechoux E. (2007) Modeling of adsorption isotherms of phenol and chlorophenols onto granular activated carbon. Part I. Two parameter models and equations allowing determination of thermodynamic parameters. *Journal of Hazardous Materials*, **147**, 381–394.

Hao Y., Yan L., Yu H., Yang K., Yu S., Shan R. & Du B. (2014) Comparative study on adsorption of basic and acid dyes by hydroxy-aluminum pillared bentonite. *Journal of Molecular Liquids*, **199**, 202–207.

Hassan H. & Hameed B.H. (2011) Fe-clay as effective heterogeneous Fenton catalyst for the decolorization of reactive blue 4. *Chemical Engineering Journal*, **171**, 912–918.

He J., Dai J., Zhang T., Sun J., Xie A., Tian S. *et al.* (2016) Preparation of highly porous carbon from sustainable αcellulose for superior performance removal of tetracycline and sulfamethazine from water. *RSC Advances*, **6**, 28023–28033.

He K., Chen G., Zeng G., Chen A., Huang Z., Shi J. *et al.* (2018) Enhanced removal performance for methylene blue by kaolin with graphene oxide modification. *Journal of the Taiwan Institute of Chemical Engineers*, **89**, 77–85.

Huang R., Liu Q., Zhang L. & Yang B. (2015) Utilization of cross-linked chitosan/bentonite composite in the removal of methyl orange from aqueous solution. *Water Science and Technology*, **71**, 174–182.

Huo X.X., Deng Q.F.R.T.Z. & Yuan Z.Y. (2013) Adsorption of Cu^{2+} and methyl orange from aqueous solutions by activated carbons of corncob-derived char wastes. *Environmental Science and Pollution Research*, **20**, 8521–8534.

Issa A.A., Al-Degs Y.S., Al-Ghouti M.A. & Olimat A.A.M. (2014) Studying competitive sorption behavior of methylene blue and malachite green using multivariate calibration. *Chemical Engineering Journal*, **240**, 554–564.

Jiang R., Fu Y., Zhu H., Yao J. & Xiao L. (2012) Removal of methyl orange from aqueous solutions by magnetic maghemite/chitosan nanocomposite films: adsorption kinetics and equilibrium. *Journal of Applied Polymer Science*, **125**, 540–549.

Khenifi A., Bouberka Z., Sekrane F., Kamech M. & Derriche Z. (2007) Adsorption study of an industrial dye by an organic clay. *Adsorption*, **13**, 149–158.

Kumar M. & Tamilarasan R. (2013) Modeling of experimental data for the adsorption of methyl orange from aqueous solution using a low cost activated carbon prepared from *Prosopis juliflora. Polish Journal of Chemical Technology*, **15**, 29–39.

Kushwaha A.K., Gupta N. & Chattopadhyaya M.C. (2011) Removal of cationic methylene blue and malachite green dyes from aqueous solution by waste materials of *Daucus carota. Journal of Saudi Chemical Society*, **18**, 200–207.

Leodopoulos C., Doulia D., Gimouhopoulos K. & Triantis T.M. (2012) Single and simultaneous adsorption of methyl orange and humic acid onto bentonite. *Applied Clay Science*, **70**, 84–90.

Leon G., Garcia F., Miguel B. & Bayo J. (2015) Equilibrium, kinetic and thermodynamic studies of methyl orange removal by adsorption onto granular activated carbon. *Desalination and Water Treatment*, **57**, 17104–171171.

Li D., Yang Y., Li C. & Liu Y. (2017) A mechanistic study on decontamination of methyl orange dyes from aqueous phase by mesoporous pulp waste and polyaniline. *Environmental Research*, **154**, 139–144.

Liu Z., Zhou A., Wang G. & Zhao X. (2009) Adsorption behavior of methyl orange onto modified ultrafine coal powder. *Chinese Journal of Chemical Engineering*, **17**, 942–948.

Luo Z., Gao M., Ye Y. & Yang S. (2015) Modification of reduced-charge montmorillonites by a series of Gemini surfactants: characterization and application in methyl orange removal. *Applied Surface Science*, **324**, 807–816.

Ma Q., Shen F., Lu X., Bao W. & Ma H. (2013) Studies on the adsorption behavior of methyl orange from dye wastewater onto activated clay. *Desalination and Water Treatment*, **51**, 19–21.

Mobarak M., Selim A.Q., Mohammed E.A. & Seliem M.K. (2018) A superior adsorbent of CTAB/H_2O_2 solution-modified organic carbon rich-clay for hexavalent chromium and methyl orange uptake from solutions. *Journal of Molecular Liquids*, **259**, 384–397.

Morais W.A., de Almeida A.L.P., Pereira M.R. & Fonseca J.L.C. (2008) Equilibrium and kinetic analysis of methyl orange sorption on chitosan spheres. *Carbohydrate Research*, **343**, 2489–2493.

Mouni L., Belkhiri L., Bollinger J.C., Bouzaza A., Assadi A., Tirri A. *et al.* (2018) Removal of methylene blue from aqueous solutions by adsorption on kaolin: kinetic and equilibrium studies. *Applied Clay Science*, **153**, 38–45.

Nadaroglu H., Kalkan E., Celebi N. & Tasgin E. (2015) Removal of reactive black 5 from wastewater using natural clinoptilolite modified with apolaccase. *Clay Minerals*, **50**, 65–76.

Patrulea V., Negrulescu A., Mincea M.M., Pitulice L.D., Spiridon O.B. & Ostafe V. (2013) Optimization of the removal of copper (II) ions from aqueous solution on chitosan and cross-linked chitosan beads. *Bioresources*, **8**, 1147–1165.

Rocher V., Bee A., Siaugue J.M. & Cabuil V. (2010) Dye removal from aqueous solution by magnetic alginate beads crosslinked with epichlorohydrin. *Journal of Hazardous Materials*, **178**, 434–439.

Soloman P.A., Basha C.A., Velan M., Ramamurthi V., Koteeswaran K. & Balasubramanian N. (2009) Electrochemical degradation of remazol black B dye effluent. *Clean – Soil Air Water*, **37**, 889–900.

Sui K., Li Y., Liu R., Zhang Y., Zhao X., Liang H. & Xia Y. (2012) Biocomposite fiber of calcium alginate/multi-walled carbon nanotubes with enhanced adsorption properties for ionic dyes. *Carbohydrate Polymers*, **90**, 399–406.

Tang Y., Yang R., Ma D., Zhou B., Zhu L. & Yang J. (2017) Removal of methyl orange from aqueous solution by adsorption onto a hydrogel composite. *Polymers and Polymer Composites*, **26**, 161–168.

Tomic Z.P., Logar V.P., Babic B.M., Rogan J.R. & Makreski P. (2011) Comparison of structural, textural and thermal characteristics of pure and acid treated bentonites from Aleksinac and Petrovac (Serbia), *Spectrochimica Acta Part A*, **82**, 389–395.

Trevino-Cordero H., Juarez-Aguilar L.G., Mendoza-Castillo D.I., Hernandez-Montoya V., Bonilla-Petriciolet A. & Montes-Moran M.A. (2013) Synthesis and adsorption properties of activated carbons from biomass of *Prunus domestica* and *Jacaranda mimosifolia* for the removal of heavy metals and dyes from water. *Industrial Crops and Products*, **42**, 315–323.

Wan J., Tao T., Zhang Y., Liang X., Zhou A. & Zhu C. (2016) Phosphate adsorption on novel hydrogel beads with interpenetrating network (IPN) structure in aqueous solutions: kinetics, isotherms and regeneration. *RSC Advances*, **6**, 23233–23241.

Zang W., Gao M., Shen T., Ding F. & Wang J. (2017) Facile modification of homoionic-vermiculites by a Gemini surfactant: comparative adsorption exemplified by methyl orange. *Colloids and Surfaces A*, **533**, 99–108.

Zeng L., Xie M., Zhang Q., Kang Y., Guo X., Xiao H. *et al.* (2015) Chitosan/organic rectorite composite for the magnetic uptake of methylene blue and methyl orange. *Carbohydrate Polymers*, **123**, 89–98.

Zhang G., Liu G. & Guo Y. (2011) Adsorption of methylene blue from aqueous solution onto hydrochloric acid-modified rectorite. *Journal of the Wuhan University of Technology, Materials Science Edition*, **26**, 817–822.

Zhang L., Hu P., Wang J., Liu Q. & Huang R. (2015) Adsorption of methyl orange (MO) by Zr (IV)-immobilized cross-linked chitosan/bentonite composite. *International Journal of Biological Macromolecules*, **81**, 818–827.

Zhu H.Y., Giang R. & Xiao L. (2010) Adsorption of an anionic azo dye by chitosan/kaolin/γ-Fe_2O_3 composites. *Applied Clay Science*, **48**, 522–526.